The Astrophysical Journal, 960:41 (15pp), 2024 January 1 https://doi.org/10.3847/1538-4357/ad0e6a

Shock Excitation in Narrow-line Regions Powered by AGN Outflows

Misaki Mizumoto[1], Hiroaki Sameshima[2], Naoto Kobayashi[2,3,4], Noriyuki Matsunaga[4,5], Sohei Kondo[3], Satoshi Hamano[4,6], Chikako Yasui[6], Kei Fukue[4,7], Akira Arai[8], Hideyo Kawakita[4,9], Shogo Otsubo[4,9], Giuseppe Bono[10,11], and Ivo Saviane[12]
[1] Science education research unit, University of Teacher Education Fukuoka, Akama-bunkyo-machi, Munakata, Fukuoka 811-4192, Japan
mizumoto-m@fukuoka-edu.ac.jp
[2] Institute of Astronomy, Graduate School of Science, The University of Tokyo, Osawa, Mitaka, Tokyo 181-0015, Japan
[3] Kiso Observatory, Institute of Astronomy, School of Science, The University of Tokyo, Mitake, Kiso-machi, Kiso-gun, Nagano 397-0101, Japan
[4] Laboratory of Infrared High-resolution Spectroscopy (LIH), Koyama Astronomical Observatory, Kyoto Sangyo University, Motoyama, Kamigamo, Kita-ku, Kyoto 603-8555, Japan
[5] Department of Astronomy, Graduate School of Science, The University of Tokyo, Hongo, Bunkyo-ku, Tokyo 113-0033, Japan
[6] National Astronomical Observatory of Japan, Osawa, Mitaka, Tokyo 181-8588, Japan
[7] Education Center for Medicine and Nursing, Shiga University of Medical Science, Seta Tsukinowa-cho, Otsu, Shiga 520-2192, Japan
[8] Subaru Telescope, National Astronomical Observatory of Japan, 650 North Aohoku Place, Hilo, HI 96720, USA
[9] Department of Physics, Faculty of Science, Kyoto Sangyo University, Motoyama, Kamigamo, Kita-ku, Kyoto 603-8555, Japan
[10] Dipartimento di Fisica, Università di Roma Tor Vergata, via della Ricerca Scientifica 1, I-00133 Roma, Italy
[11] INAF-Osservatorio Astronomico di Roma, via Frascati 33, I-00078 Monte Porzio Catone, Italy
[12] European Southern Observatory, Alonso de Cordova 3107, Santiago, Chile

Received 2021 November 24; revised 2023 November 18; accepted 2023 November 19; published 2023 December 21

Abstract

Outflows in an active galactic nucleus (AGN) are considered to play a key role in the evolution of the host galaxy through transfer of a large amount of energy. A narrow-line region (NLR) in the AGN is composed of ionized gas extending from parsec to kiloparsec scales. It has been suggested that shocks are required to ionize the NLR gas. If AGN outflows generate these shocks, they will sweep through the NLR, and the outflow energy will be transferred into a galaxy-scale region. In order to study the contribution of the AGN outflow to the NLR-scale shock, we measure the [Fe II]λ12570/[P II]λ11886 line ratio, which is a good tracer of shocks, using near-infrared spectroscopic observations with the Warm INfrared Echelle spectrograph to Realize Extreme Dispersion and sensitivity (WINERED) mounted on the New Technology Telescope. In 13 Seyfert galaxies we observed, the [Fe II] and [P II] lines were detected in 12 and 6 targets, respectively. The [Fe II]/[P II] ratios in 4 targets were found to be higher than 10, which implies the existence of shocks. We also found that the shock is likely to exist where an ionized outflow, i.e., a blue wing in [S III]λ9533, is present. Our result implies that the ionized outflow present in an NLR-scale region sweeps through the interstellar medium and generates a shock.

Unified Astronomy Thesaurus concepts: Active galaxies (17)

1. Introduction

The influence of an active galactic nucleus (AGN) on the evolution of its host galaxy has been actively studied in recent decades (Harrison et al. 2018 for review). One example is the correlation of the mass of the central supermassive black hole (SMBH) and the velocity dispersion of the galactic spheroids (i.e., bulges and elliptical galaxies; Ferrarese & Merritt 2000; Gebhardt et al. 2000). The fact that there is a positive correlation between them implies their coevolution, that is, SMBHs control the evolution of their host galaxies, and vice versa. Theoretical studies predict that AGN outflows, which originate from the radiation pressure due to accretion onto the black hole, offer "a plausible physical origin" (King & Pounds 2015) for the coevolution. The impact of the AGN on the host galaxy has also been implemented by many cosmological hydrodynamical simulations, such as the EAGLE project (Booth & Schaye 2009; Crain et al. 2015; Schaye et al. 2015), the SIMBA project (Davé et al. 2019; Thomas et al. 2019; Appleby et al. 2020), and the IllustrisTNG project (Weinberger et al. 2017; Pillepich et al. 2018; Weinberger et al. 2018; Nelson et al. 2019).

The AGN outflows have a wide variety of velocities and size scales. For example, in the innermost part ($\lesssim 10^{-3}$ pc), ultrafast outflows (UFO) with a velocity of 10%–30% of the light speed are observed in X-rays (e.g., King & Pounds 2003; Pounds et al. 2003; Reeves et al. 2003; Tombesi et al. 2010; Gofford et al. 2013; Tombesi et al. 2014). Their kinetic power usually exceeds the binding energy of the galactic spheroids by ∼3 mag (see Equations (5) and (6) in King & Pounds 2015). In the outer regions, multiphase outflows are also observed; one example is an ionized outflow that is slower (several hundred km s^{-1}) and more extended (∼1 kpc; e.g., Rupke et al. 2005; Komossa et al. 2008; Müller-Sánchez et al. 2011; Liu et al. 2013; Harrison et al. 2014; Karouzos et al. 2016; Davies et al. 2020; Singha et al. 2022). They are often observed as a blueshifted excess component (blue wing; Komossa et al. 2008) in the optical [O III]λ5007 line. Recent studies have suggested that they are driven by AGN radiation at ∼1 pc and travel up to ∼1 kpc (Wada et al. 2018; Meena et al. 2021).

In this work, we focus on the physical processes in and around a narrow-line region (NLR). The NLR extends from parsec to kiloparsec scales and emits forbidden lines with a line width of several hundred km s^{-1} (Peterson 1997). The main ionization mechanism in the NLR is photoionization from the AGN radiation (Ho et al. 1993). However, it is known that photoionization cannot explain all the observed line features (e.g., Simpson et al. 1996), and instead of this or in addition to it, shocks are likely to cause some features (e.g., Knop et al. 1996; Wilson & Raymond 1999; Mouri et al. 2000; Rodríguez-Ardila et al. 2004). Here, we developed a scenario in which a shock triggered by the AGN outflow contributes to the NLR ionization; the fast velocity of the AGN outflow will generate the shock by interaction with the interstellar medium (ISM; e.g., Richings & Faucher-Giguère 2018a, 2018b). The shock may make a critical contribution to the NLR ionization by transferring energy from the AGN to the NLR-scale cloud (i.e., the spheroid-scale cloud). In these manners, the AGN outflow can carry its energy to the spheroid. Some studies have partially supported this scenario; for example, Joh et al. (2021) found that the gas density and velocity dispersion in the NLR region are higher when the AGN is more active, which implies that NLR gas clouds are brought from the AGN outflows.

To investigate the existence of shocks in the NLR, Terao et al. (2016, T16) studied the flux ratio of the [Fe II]λ12570 and [P II]λ11886 emission lines observed in the near-infrared (NIR) J band. Oliva et al. (2001) proposed that the line flux ratio of [Fe II] to [P II] is a good tracer of shocks. The two lines share similar critical densities and ionization potentials, and they are expected to be excited in similar physical environments. By contrast, dust depletions are very different (Hobbs et al. 1993); iron is abundant in dust, whereas phosphorus is almost absent. When a shock breaks dust, [Fe II] appears to be much stronger than [P II]. Indeed, it is known that [Fe II] is much stronger in supernova remnants than [P II], where shocks are present, whereas both have about the same flux in the Orion bar, where there are no known shocks (Oliva et al. 2001). T16 investigated the line ratios of 44 Seyfert galaxies (including some data taken from the literature) and found that three of them (NGC 2782, NGC 5005, and Mrk 463) have [Fe II]/[P II] ratios higher than 10, whereas more than half of them have a lower ratio ($\sim$2). They also found that the line ratios are not correlated with the radio-loudness or starburst intensity, suggesting that the mechanism that might trigger the shock is the AGN outflow.

The goal of this paper is to study the validity of our scenario that the AGN parsec-scale outflow generates the shock in the NLR. We describe our sample selection, observation setup, and data reduction in Section 2. The obtained line profiles are explained in Section 3. We discuss how the shocks are generated in NLRs in Section 4 and summarize our result in Section 5.

2. Observations and Data Reduction

2.1. Target Selection and Observations

The observations were carried out with the Warm INfrared Echelle spectrograph to Realize Extreme Dispersion and sensitivity (WINERED[13]; Ikeda et al. 2016, 2022) mounted on the New Technology Telescope (NTT) at the La Silla observatory as a visitor instrument. WINERED has a bandwidth of 9100–13500 Å. The slit length is 16.″34, and the pixel scale is 0.″27 pixel^{-1}. The slit width was set to 1.″08 (=4.0 pixel; WIDE mode) with $R = 18{,}000$ ($\Delta v = 17$ km s^{-1}). The observations were carried out for five nights between 2017 November 30 and 2018 March 3, with a seeing of 0.″7–1.″5.

The X-ray UFO catalog papers (Tombesi et al. 2010; Gofford et al. 2013; Tombesi et al. 2014) listed 36 objects. Of these, 11 objects can match our selection thresholds; they are located in the southern sky and have Jmag < 15.5 and $z < 0.07$, for which the spectral lines of interest ([Fe II]λ12570 and [P II] λ11886) fall in the observable wavelength range. In addition, two Seyfert galaxies, 1H 0707–495 and IRAS 13224−3809, have been reported to host strong UFOs (Hagino et al. 2016; Parker et al. 2017). Thus we also observed them; the total number of targets is 13.[14] We also note that all of them are radio-quiet ($\log R < 1$, where R is the ratio of the flux density at 5 GHz to 4400 Å), that is, we can exclude potential energy inputs from radio jets and study the influence of multiscale outflows. Tables 1 and 2 show the target list and the observation log, respectively.

When the emission of the host galaxy was anticipated to potentially occupy most of the slit length of 16.″34, we used the object-sky-object mode (OSO mode), that is, the blank sky was observed between the object observations. No bright sources were observed immediately before the targeted observations to avoid persistence (see Section 5.3 in Ikeda et al. 2022). Where necessary, we waited until the persistence was sufficiently low before we started observing the targets.

When a target did not occupy the slit length, we adopted the ABBA mode. In this mode, we positioned the object at a location offset from the center of the slit (designated as position A), and then, for the next exposure, we positioned it at a location shifted in the opposite direction (designated as position B). By subtracting the spectra obtained from these two positions (i.e., A–B or B–A), the contribution of the sky background is removed and we obtain an image with two spectra, one positive and one negative. In order to discuss the NLR in AGN with a spatial extent on kiloparsec scales, only those with a throw distance (distance between the centroids of the A and B exposures) exceeding 2 kpc are treated in this mode.

The data reduction was performed using IRAF[15] and PyRAF.[16]

2.2. Data Reduction

The detailed explanation of the data reduction (e.g., wavelength calibration, dispersion calibration, and flat-fielding) in WINERED are described in Section 8 in Ikeda et al. (2022). Hereafter, the data reduction unique to this paper is explained.

The source region was selected in the following steps. First, a spatial profile along the slit length was plotted and the peak was searched (vertical red lines in Figure 1). Next, the spatial profile around the peak was fit with a single Gaussian to calculate the full width at half maximum (FWHM). Last, the source region was selected from $-1 \times$ FWHM to $+1 \times$ FWHM (red shaded regions in Figures 1). The sky spectrum was set to have the same width as the source

---

[13] The raw data on WINERED were generated at Kyoto Sangyo University. The derived data and relevant reduction scripts underlying this article are available from the corresponding author on reasonable request.

[14] Although NGC 5506 also meets these criteria, we decided not to use it in this paper because of a defect in the observation data.

[15] IRAF is distributed by the National Optical Astronomy Observatories, which is operated by the Association of Universities for Research in Astronomy, Inc. (AURA) under cooperative agreement with the National Science Foundation.

[16] PyRAF is a product of the Space Telescope Science Institute, which is operated by AURA for NASA.

Table 1
Target List

Name (1)	Redshift (2)	Type (3)	$f_{\rm opt}$ (mJy) (4)	$f_{\rm radio}$ (mJy) (5)	log(R) (6)	log($\dot{M}_{\rm UFO}$) (g s^{-1}) (7)	log($K_{\rm UFO}$) (erg s^{-1}) (8)	References (9)
1H 0707–495	0.0406	Sy 1	3	$<1.6^{\rm a}$	<-0.3	∼25.0	∼44.3	Hagino et al. (2016)
Ark 120	0.0327	Sy 1	7.9	3	−0.4	>23.5	>43.1	Tombesi et al. (2012)
ESO 323-G77	0.0150	Sy 2	16	$36^{\rm b}$	0.4	25.3 ± 0.7	42.1 ± 0.7	Tombesi et al. (2012)
IC 4329A	0.0161	Sy 1	13	$67^{\rm b}$	0.7	>24.2	>42.8	Tombesi et al. (2012)
IRAS 13224–3809	0.0658	Sy 1	1.0	$5.4^{\rm b}$	0.8	24.8 − 25.5	44.4 − 44.8	Chartas & Canas (2018)
MCG–5–23–16	0.0085	Sy 2	10	6	−0.2	23.9 ± 1.0	42.7 ± 1.0	Tombesi et al. (2012)
MCG–6–30–15	0.0078	Sy 1	10	1	−1.0	23.8 ± 0.3	40.1 ± 0.3	Gofford et al. (2015)
NGC 1068	0.0038	Sy 2	0.6	2.2	0.6	$24.1^{+0.2}_{-0.3}$	$43.6^{+0.2}_{-0.3}$	Mizumoto et al. (2019)
NGC 1365	0.0055	Sy 1	350	180	−0.3	24.1 ± 0.1	40.5 ± 0.1	Gofford et al. (2015)
NGC 3783	0.0097	Sy 1	40	13	−0.5	>24.2	<40.5	Gofford et al. (2015)
NGC 4507	0.0118	Sy 2	25	11	−0.4	>21.9	>41.2	Tombesi et al. (2012)
NGC 6240	0.0243	Sy 2	20	170	0.9	$26.1^{+0.3}$	$44.9^{+0.3}$	Mizumoto et al. (2019)
NGC 7582	0.0053	Sy 2	140	110	−0.1	23.8 ± 1.0	43.4 ± 1.1	Tombesi et al. (2012)

Notes. (1) Target name. (2) Redshift. (3) AGN type based on the optical spectra. Sy 1/2 means Seyfert 1/2 galaxy, respectively. (4) Flux density at 4400 Å (Véron-Cetty & Véron 2010). (5) Flux density at 5 GHz (Véron-Cetty & Véron 2010) unless otherwise noted.

[a] Upper limit measured as a root mean square using the Giant Metrewave Radio Telescope (GMRT) 150 MHz all-sky radio survey data (Intema et al. 2017).

[b] Flux density at 1.4 GHz. (6) Radio-loudness ($f_{\rm radio}/f_{\rm opt}$). (7) UFO mass-loss rate. (8) UFO kinetic power. (9) References for (7) and (8).

spectrum. We used Skycorr (Noll et al. 2014) to subtract the sky spectrum because the infrared background can change substantially. The sky-subtracted spectra were normalized to unity for the continuum, using the `continuum` command in PyRAF. In the `continuum` command, the spectra were normalized by a cubic Legendre polynomial, without emission- or absorption-line-dominant bands. As a next step, the telluric absorption lines were corrected for with the `telluric` command, using A0-type standard stars with a similar airmass that were observed before or after a suite of observations (Table 2). In the `telluric` command, we determined the optimal value of the scale and wavelength shift of the telluric standard spectrum after removing intrinsic lines (see Sameshima et al. 2018 for the detailed method with which the intrinsic lines were removed) and divided it by the target spectrum.

The targets presented in this study have a low redshift. Therefore, it is imperative to prevent the extended signal of a galaxy from contaminating the sky background, which is then subtracted from each of the pair of positions A and B positions. Column (5) in Table 3 provides insights into the size of the spectral extraction region, which is a product of Gaussian fitting as illustrated in Figure 1. The spatial extension of the emission region along the slit length falls within the range of 9–13 pixels for the ABBA mode. Although it is worth noting that this spatial extent is determined using the NIR continuum and may not be entirely congruent with the NLR extent, which should ideally be assessed via narrow lines, we maintain confidence that oversubtraction was effectively mitigated in the A–B sky-subtraction process. This confidence is supported by the fact that most of the emission resides within this defined region, and the spatial extent (9–13 pixels for the A–B subtraction) remains significantly smaller than the throw distance of 45 pixels by a factor exceeding three. Figure 2 visually exemplifies the spectral extraction region and the sky region, reaffirming that extended emission in position A does not contaminate position B, and vice versa.

Because we are interested in the line-intensity ratio and in the shape of the line profile, we did not observe the flux of the standard star to measure the absolute value of the flux. Then, all the exposures were stacked, and the continuum of the total spectrum was normalized again. As the last step, the barycentric correction was performed.

3. Results

3.1. The [Fe II] and [P II] Lines

The obtained line profiles of [Fe II] and [P II] are shown in Figure 3. The line fitting was performed with the Markov chain Monte Carlo methods (MCMC) using the emcee module (Foreman-Mackey et al. 2013) in Python. We set the number of independent chains (walkers) to explore the parameter space (nwalker) to be 512, and the number of iterations performed by each walker in the MCMC process (niter) to be 3000. The fitting procedure is as follows: (1) One positive Gaussian was introduced. The line width (standard deviation; σ_v) was set to be larger than the velocity resolution of 17 km s^{-1}. Because the line center may be slightly shifted due to gas motion, the central velocity was set to be free within ±200 km s^{-1} from the rest frame. We summarize the line intensity in Table 4 as an equivalent width (EW). Its error (1σ) was calculated from the Bayesian posterior probability (see Figure 11 in Appendix B for the corner plots of the MCMC fitting). The adjacent [S IX] emission line was simultaneously modeled for the fitting of [Fe II] in IC 4329A because the fitting model was distorted without it. (2) If the line intensity did not exceed three times its error, the line was considered undetectable, and three times the error was adopted as the upper limit. (3) If some residuals were seen after introducing the first Gaussian and they overlapped with the line of interest, additional Gaussians were introduced ([Fe II] in NGC 4507 and [P II] in NGC 6240). To determine whether the additional Gaussian was necessary, an F-test (Bevington 1969; Eadie et al. 1971) was performed based on the chi-squared and the degrees of freedom before and after the Gaussian was added. The additional Gaussian was only introduced when it was judged to be necessary at the 99.7% confidence level. This procedure was not performed when the

Table 2
Observation Log

Name (1)	Date (2)	Airmass (3)	Mode (4)	Exposure (sec × freq.) (5)	Std. Star (6)	Airmass of Std. Star (7)	Seeing (arcsec) (8)
1H 0707−495	2017 Nov 30	1.07–1.08	ABBA	750 × 4	60 Ori	1.15	1.48
Ark 120	2017 Nov 30	1.15–1.17	ABBA	900 × 4	60 Ori	1.15	1.48
ESO 323-G77	2018 Mar 1	1.03–1.05	AB	900 × 2	HD 139129	1.09	0.93
IC 4329A	2018 Mar 2	1.05–1.07	ABA	300 × 3	HD 139129	1.09	0.71
IRAS 13224−3809	2018 Mar 2	1.03–1.06	ABBA ABBA	900 × 8	HD 139129	1.09	0.71
MCG −5-23-16	2018 Mar 1	1.22–1.43	ABBA	900 × 4	HD 103101	1.42	0.84
MCG −6-30-15	2018 Mar 3	1.01–1.02	ABBA	600 × 4	HD 118054	1.04	1.02
NGC 1068	2017 Nov 30	1.16–1.20	OSO	900 × 2	60 Ori	1.15	1.48
NGC 1365	2017 Nov 30	1.02–1.10	OSO OS	900 × 3	60 Ori	1.15	1.48
NGC 3783	2018 Feb 28	1.15–1.20	AB	900 × 2	F Pup	1.20	0.85
NGC 4507	2018 Mar 3	1.02–1.04	OSO	900 × 2	HD 118054	1.04	1.02
NGC 6240	2018 Mar 3	1.31–1.38	OSO	900 × 2	21 Oph	1.23	0.77
NGC 7582	2017 Nov 30	1.07–1.11	OSO	900 × 2	60 Ori	1.15	1.48

Note. (1) Target name. (2) Observation date. (3) Airmass (minimum–maximum) (4) Observation mode. A/B shows positions A and B, and O/S shows the object and sky observation. (5) (Exposure time in seconds for each snapshot) × (the number of snapshots). (6) Name of the telluric standard star. (7) Airmass of the telluric standard star. (8) Seeing of the telluric standard star.

residuals were space sufficiently far apart to be unaffected by fitting of the line of interest (e.g., [Fe II] in NGC 3783).

The EW ratios of [Fe II] to [P II], as well as the obtained EW and σ_v of each line, are listed in Table 4. We detected the [Fe II] line in 12 out of 13 AGNs and [P II] in 6 of them. Neither of the lines was detected in NGC 1365.

While T16 calculated the [Fe II]/[P II] ratios using the line fluxes, we use the EWs. Our ratios must be $F_{\lambda,\mathrm{[Fe\,II]}}/F_{\lambda,\mathrm{[P\,II]}}$ times higher than those of T16, where $F_{\lambda,k}$ refers to the continuum flux density at the k line. The NIR power-law slope in the wavelength unit (α_λ, where $F_\lambda \propto \lambda^{\alpha_\lambda}$) in the quasar composite spectrum is known to be $\alpha_\lambda = -0.19$ (Glikman et al. 2006). If the slope in Seyfert galaxies is similar to those in quasars, the factor is $F_{\lambda,\mathrm{[Fe\,II]}}/F_{\lambda,\mathrm{[P\,II]}} = (1.257/1.188)^{-0.19} = 0.99$. Therefore, the difference of the line ratio definitions by us and T16 hardly affects the results.

We found that four sources (Ark 120, ESO 323-G77, MCG −5-23-16, and NGC 4507) have higher [Fe II]/[P II] ratios than 10; notably, for NGC 4507, [P II] was detected and the ratio exceeded 10, which is the first report. They are likely to have shocks in the NLR. This result doubles the number of known AGN samples with a line ratio higher than 10, where most major previous work was done by T16.

3.2. The [S III] Line

We use the [S III]λ9533 line as a tracer of the ionized outflow instead of the conventional optical [O III]λ5007 line. The two lines share the same transition ($^3P_2$–$^1D_2$) and belong to the same family in the periodic table. It is predicted that they are emitted from a similar region in the AGN (see, e.g., Liu et al. 2015). We also note that sulfur is an almost perfect volatile element because it is not locked in dust and thus is suitable for tracing the pure outflow component. Figure 4 shows the obtained [S III]λ9533 line profiles. The fitting procedure is almost the same as in Figure 3, but the line center is allowed to be ±1000 km s^{-1} because the gas motion traced by the [S III] may be larger. The first Gaussian to be introduced, whose line velocity is almost zero in the rest frame, is referred to as the "main" Gaussian, and the additional Gaussians are "sub." If the center velocity of the sub-Gaussian was negative (within a range of −1000 to 0 km s^{-1}) at the 99.7% confidence level, it was interpreted as the blue wing, and we categorized the object as having ionized outflow. Consequently, in 6 out of the 13 AGNs (Ark 120, IRAS 13224−3809, MCG −5-23-16, NGC 1068, NGC 4507, and NGC 7582), the blue wing is detected. Table 4 lists the fitting results, including the velocity shifts, σ_v, and EWs.

3.3. Absorption Features around the [P II] Line

Some absorption features were apparent in some AGNs around the [P II] line. In particular, those at $v = -1400$ km s^{-1} and +200 km s^{-1} (corresponding to 11830 Å and 11895 Å, respectively) were observed in multiple sources: the 11830 Å line in MCG −5-23-16, MCG −6-30-15, NGC 1068, NGC 1365, NGC 4507, and NGC 7582, and the 11895 Å line in ESO 323-G77, NGC 1365, and NGC 7582. These lines cannot be the remaining counts of the telluric absorption because some of them are seen in the wavelength range in which any potential remaining effect is small. They were broader than the telluric lines and instrumental resolution. Therefore, they are not artificial. They were located at a similar wavelength in the rest frame of each AGN, implying that they are associated with AGNs and not with the Galactic absorption. Interestingly, they were mostly present in Seyfert 2 galaxies; the exceptions are MCG −6-30-15 (which has complex absorbers close to the central SMBH; Lee et al. 2001) and NGC 1365 (whose broad Hα line is extremely faint, and which is classified as Seyfert 1.9; Trippe et al. 2010. This implies that most of the broad-line region may be covered). Consequently, we suggest that these absorptions are due to molecular gas in the torus or to some obscuring material (e.g., polar dust; Hönig et al. 2013) in the vicinity of the AGNs. The line identification and search for other features will be presented in our forthcoming paper.

3.4. Spatial Distribution of the [Fe II]/[P II] Ratio in NGC 1068

NGC 1068 is the brightest and most nearby target and is thus suitable for studying the position dependence on the [Fe II]/[P II] ratio. It was reported that whereas the [Fe II]/[P II] ratio is low (∼1) near the central core, it increases to ∼7 at a distance

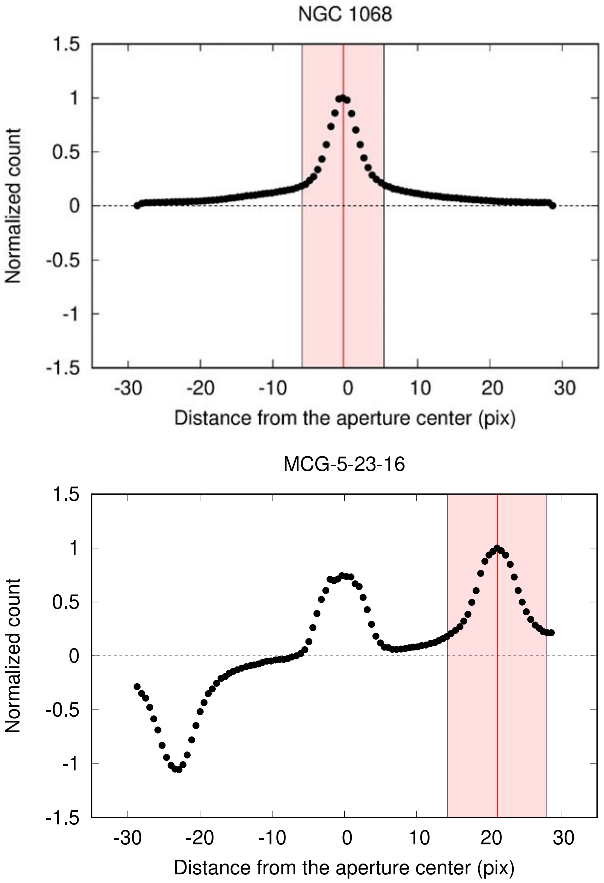

Figure 1. Spatial profiles of the emission along the slit. The upper panel shows NGC 1068, in which the blank sky was observed between the object observations for the sky subtraction. The profile shows the one in the object observation. The source region at the center is automatically selected with a Gaussian fitting. The lower panel shows MCG–5-23-16, in which the image of position A was subtracted from the image of position B, and the one-dimensional spatial profile around the slit was calculated. The positive peak at the positive distance (right-hand side in the panel) is the signal at position A, whereas the negative one on the left-hand side is for position B. The spectrum extraction region (red) is automatically selected, as in the upper panel. The peak at the center is the remaining counts from a bright telluric standard star that was observed shortly before this target observation.

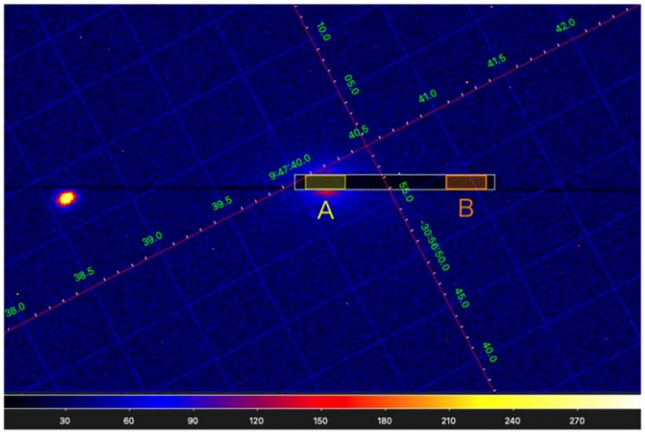

Figure 2. The slit-viewer image of MCG–5-23-26 (position A). The left and right sides are reversed from Figure 1. The white, yellow shaded, and orange shaded rectangles show the WINERED slit, the spectral extraction region (position A), and the sky region (position B), respectively. We note that the yellow shaded rectangle corresponds to the red shaded region in Figure 1. The signal on the left is a serendipitous point source (2MASS J09473861–3057050).

of 2″–4″ from the center (Hashimoto et al. 2011; Riffel et al. 2014). In order to confirm this spatial dependence in our observation, we created spectra divided into the slit-length direction and calculated the EWs of the two emission lines. The continuum peak position was set as the origin, and the spectra were extracted from every 5 pixels (=1″35; almost equivalent to the seeing). The position angle was 220 deg, and the slit was oriented roughly from southeast to northwest. Eleven spectra were derived, covering 7″5 on each side in total. Whereas the [Fe II] emission lines were detected in all of them, the [P II] emission lines were detected in only the three central lines. The EW values or their upper limits were calculated in the same way as in Section 3.1. The width of the undetected [P II] lines used for the upper limit was the same as for the spectrum in the central bin. The obtained spatial dependence of the [Fe II]/[P II] ratio is shown in Figure 5. As in previous studies (Hashimoto et al. 2011; Riffel et al. 2014), we confirmed that the ratio is lower at the center and higher at a projected distance of ∼3″. This means that photoionization is dominant in the vicinity of the core in NGC 1068, while the shock ionization appears farther from the core.

4. Discussion

4.1. The [Fe II]/[P II] Ratio

Figure 6 shows the relation between the EWs of the two emission lines, [Fe II] and [P II]. All the sources for which [P II] is not detected only show a weak [Fe II] line. This suggests that the nondetection of [P II] is simply because the narrow lines are weak regardless of the species and are not due to the shock. The detection of weak [P II] emission lines is critical for an accurate measurement of the [Fe II]/[P II] ratio. For example, the weakest [P II] line detected in T16 (NGC 5506) has an EW of ∼1.8 Å (this value is not very accurate because it is read from the spectrum figure). On the other hand, our study can detect the emission line with EW = 0.49 Å (NGC 4507), which is 3.6 times fainter than the detection limit of T16. For example, if the detection limit of the [P II] line were 1.8 Å in NGC 4507 as in T16, then the [P II] line could not be detected and the ratio value would only have a lower limit of >6.7. In this case, we would not be able to conclude whether the shock exists. Consequently, our observation provides a more robust conclusion on the existence of the shock than the previous study.

Figure 7 compares the [Fe II]/[P II] ratios with the radio-loudness. The result of T16 is also superposed. T16 found that no significant difference exists between the average value of the [Fe II]/[P II] ratios in the radio-loud AGNs ($R > 10$; the average value is 3.67 ± 1.09) and that in the radio-quiet AGNs ($R < 10$; the average value is 2.87 ± 1.38) for the [P II]-detected objects, and stated that the radio jet is unlikely to be the main contributor to the shock in the NLR. We performed a Kolmogorov–Smirnov (KS) test to quantitatively compare the distributions of the [Fe II]/[P II] ratios in this study and in T16. Only the [P II]-detected sources were used. The obtained p-value was 0.562, so that we cannot discuss any significant differences in this sample.

Table 3
Pixel Scale, Spectral Extraction Region, and Throw Distance of Each Target

Name (1)	Pixel Scale (pc pixel^{-1}) (2)	Spectral Extraction Region (arcsec × arcsec) (3)	 (pc × pc) (4)	 (pix × pix (5)	Throw Distance (kpc) (6)
1H 0707−495	2.2×10^2	2.70 × 1.08	$(2.2 \times 10^3) \times (8.7 \times 10^2)$	10 × 4	9.8
Ark 120	1.8×10^2	2.43 × 1.08	$(1.6 \times 10^3) \times (7.1 \times 10^2)$	9 × 4	8.0
ESO 323-G77	8.3×10^1	2.43 × 1.08	$(7.5 \times 10^2) \times (3.3 \times 10^2)$	9 × 4	3.7
IC 4329A	8.9×10^1	2.43 × 1.08	$(8.0 \times 10^2) \times (3.6 \times 10^2)$	9 × 4	4.0
IRAS 13224−3809	3.4×10^2	2.70 × 1.08	$(3.4 \times 10^3) \times (1.4 \times 10^3)$	10 × 4	15
MCG −5-23-16	4.7×10^1	3.51 × 1.08	$(6.2 \times 10^2) \times (1.9 \times 10^2)$	13 × 4	2.1
MCG −6-30-15	4.4×10^1	2.70 × 1.08	$(4.4 \times 10^2) \times (1.7 \times 10^2)$	10 × 4	2.0
NGC 1068	1.3×10^1	2.97 × 1.08	$(1.4 \times 10^2) \times (5.2 \times 10^1)$	11 × 4	⋯
NGC 1365	2.4×10^1	3.24 × 1.08	$(2.8 \times 10^2) \times (9.4 \times 10^1)$	12 × 4	⋯
NGC 3783	5.4×10^1	2.97 × 1.08	$(6.0 \times 10^2) \times (2.2 \times 10^2)$	11 × 4	2.4
NGC 4507	6.6×10^1	4.05 × 1.08	$(9.8 \times 10^2) \times (2.6 \times 10^2)$	15 × 4	⋯
NGC 6240	1.3×10^2	2.70 × 1.08	$(1.3 \times 10^3) \times (5.3 \times 10^2)$	10 × 4	⋯
NGC 7582	2.9×10^1	4.32 × 1.08	$(4.6 \times 10^2) \times (1.2 \times 10^2)$	16 × 4	⋯

Note. (1) Target name. (2) Pixel scale. (3)–(5) Region used to extract the spectrum (along the slit length) × (slit width). (6) Distance between the centroids of exposures A and B. This corresponds to 45 pixels or $12\rlap{.}''15$.

4.2. UFO Contribution

To study the UFO contribution to the shock, we compare the UFO mass-loss rate and kinetic power with the [Fe II]/[P II] ratios in Figure 8. Using the four objects for which both UFO parameters and the [Fe II]/[P II] ratios were determined (NGC 7582, NGC 1068, IRAS 13224–3809, and NGC 6240), we examined their correlations. The Pearson correlation coefficient values and p-values were –0.465 and 0.535 for the log mass-loss rate and –0.368 and 0.632 for the log UFO power, respectively. Thus, no correlations were detected between them.

While the UFO is considered to sweep through the ISM and produce a kiloparsec-scale outflow (e.g., Tombesi et al. 2015; Marasco et al. 2020), the efficiency of the kinetic power transfer from the UFO to the kiloparsec-scale outflow varies widely, depending on the flow type. Notably, it can be in the energy-conserving or momentum-conserving modes (see, e.g., Mizumoto et al. 2019). If these two types exist in the sample, no correlation is observed even when UFOs contribute to some (indirect) extent to the kiloparsec-scale outflows and shocks. If only AGNs with energy-conserving flows were selected, a correlation between UFOs and NLR-scale shocks might be identified. Our sample size, however, is too small to conduct this type of study. The flow type from subparsec to kiloparsec scales needs to be determined for a direct assessment of the effect of UFOs on shocks.

4.3. Correlation with the [S III] Outflow

Figure 9 shows the obtained relation between the [S III] outflow velocity, that is, the velocity shift in the center of the blue wing from the rest frame if the source has an outflow, and the line ratio. We use the off-centered value for NGC 1068. There is an indication that targets associated with [S III] outflows have a higher [Fe II]/[P II] ratio, that is, they are more likely to produce shocks.

As discussed in Section 3.4, the [Fe II]/[P II] ratio of NGC 1068 is higher (∼7) at an angular distance of ∼3″, but low (<1) within 1″ from the center. In addition, integral field unit (IFU) observations revealed an annulus of $r \sim 2''$ with a high [Fe II]/[P II] ratio (∼5–8), whereas the inner circular region of $r < 1''$ has a low ratio ($\lesssim 2$). These off-centered, high [Fe II]/[P II] regions have been also found in other AGNs (e.g., Storchi-Bergmann et al. 2009; Schönell et al. 2019; Riffel et al. 2020). When we use the [Fe II]/[P II] ratio in the off-centered region (see Figure 5), the ratio is similar to the ratios in the other objects with [S III] outflows (see the open red circle in Figure 9). Consequently, all the AGNs with the NLR-scale outflows are found to have a high [Fe II]/[P II] ratio of $\gtrsim 7$ in our sample, and thus the ionized outflows are considered to play a dominant role in the shock ionization.

In addition, we note that the [Fe II]/[P II] peak region in NGC 1068 reported by Riffel et al. (2014) and the [O III] spatial distribution shown by Das et al. (2006) share a similar size scale. The [O III] emission region is extended in the northeast direction with a radius of 0″–2″ (Das et al. 2006). This means that the ionized outflow is blown from the AGN core in this direction. On the other hand, the annulus with the high [Fe II]/[P II] ratio ($r \sim 2''$–$3''$) is asymmetrical, and the shock is more prominent in the northeast part (Riffel et al. 2014). This geometry matches our scenario in which the AGN-ionized outflow triggers the shock ionization, as shown in Figure 10. Based on this picture, the kinetic energy or the momentum flux of the ionized outflow triggered by the AGN are transferred to the gas in a region of several hundred parsecs via the shock. In other words, the AGN feedback (i.e., the AGN affects the host galaxy via the outflow) occurs in the NLR via the ionized outflow and the shock.

The exception is ESO 323-G77, which is not associated with the [S III] outflows, but has a ratio higher than 10. The [S III] emission line of ESO 323-G77 shows an asymmetric profile, which is present in this source alone in our sample (Figure 4). If the asymmetry originates in the outward motion of the NLR cloud in a dusty region (Peterson 1997), this bulk motion may cause some shock ionization. Another possible scenario is that a potential dusty wind, the presence of which was suggested based on the detection of dust emission extending axially in this source (Leftley et al. 2018), generates the shocks. In any case, some outflowing gas may exist in ESO 323-G77.

Table 4

Results of the NTT/WINERED Observations

Name (1)	[Fe II] EW (Å) (2)	[Fe II] σ_v (km s^{-1}) (3)	[P II] EW (Å) (4)	[P II] σ_v (km s^{-1}) (5)	[Fe II]/[P II] (6)	[S III]$_{\rm peak}$ EW (Å) (7)	[S III]$_{\rm peak}$ σ_v (km s^{-1}) (8)	[S III]$_{\rm wing}$ EW (Å) (9)	[S III]$_{\rm wing}$ velocity (km s^{-1}) (10)	[S III]$_{\rm wing}$ σ_v (km s^{-1}) (11)
1H 0707−495	0.58 ± 0.07	75^{+13}_{-10}	<0.32	⋯	>1.8	2.6 ± 0.2	⋯	⋯	⋯	⋯
Ark 120	0.54 ± 0.03	144 ± 9	<0.027	⋯	>20.0	3.8 ± 0.5	173 ± 6	0.85 ± 0.52	−310 ± 90	200 ± 50
ESO 323-G77	0.91 ± 0.04	184^{+10}_{-9}	<0.075	⋯	>12.2	6.0 ± 0.2	200 ± 10	⋯	⋯	⋯
IC4329A	2.04 ± 0.14	240 ± 10	1.09 ± 0.12	390 ± 50	1.87 ± 0.24	26.4 ± 0.2	235 ± 2	⋯	⋯	⋯
IRAS 13224−3809	0.95 ± 0.06	94 ± 6	<0.20	⋯	>4.9	1.17 ± 0.06	55 ± 4	7.1 ± 1.2	−217 ± 11	417 ± 9
MCG −5-23-16	0.68 ± 0.03	95^{+6}_{-5}	<0.012	⋯	>56.5	13.47 ± 0.06	83.5 ± 0.4	0.31 ± 0.02	−292 ± 3	43 ± 3
MCG −6-30-15	0.50 ± 0.04	100 ± 10	<0.12	⋯	>4.1	9.81 ± 0.06	60 ± 2	⋯	⋯	⋯
NGC 1068	6.53 ± 0.03	253 ± 1	6.53 ± 0.03	277 ± 2	1.00 ± 0.01	170.2 ± 0.3	⋯	6.91 ± 0.04	−860 ± 10	144.7 ± 0.7
NGC 1365	<0.018	⋯	<0.015	⋯	⋯	10.4 ± 0.4	⋯	⋯	⋯	⋯
NGC 3783	1.65 ± 0.06	131^{+6}_{-5}	0.51 ± 0.05	104^{+13}_{-11}	3.23 ± 0.36	19.2 ± 0.8	⋯	⋯	⋯	⋯
NGC 4507	12.1 ± 0.8	⋯	0.49 ± 0.05	70^{+10}_{-9}	25 ± 3	35.5 ± 0.7	137 ± 3	22.3 ± 0.3	−100 ± 20	400 ± 100
NGC 6240	14.64 ± 0.13	352 ± 3	12.2 ± 1.1	⋯	1.2 ± 0.1	16.2 ± 0.2	447 ± 5	⋯	⋯	⋯
NGC 7582	4.65 ± 0.04	80.6 ± 0.8	0.65 ± 0.03	51 ± 2	7.1 ± 0.3	13 ± 2	60 ± 20	7.1 ± 1.5	−120 ± 5	120 ± 2

Note. (1) Target name (2) EW of the [Fe II] line. The upper limit of three times of the error (standard deviation) is indicated for no detection. (3) The line broadening of [Fe II], which is only shown when the line is modeled by a single Gaussian. Columns (4) and (5), (7) and (8), and (9) and (11) are the same as Columns (2) and (3), but for the [P II] line, the central peak of [S III], and the blue wing of [S III], respectively. (10) Velocity shift for the line center of the [S III] blue wing from the central peak.

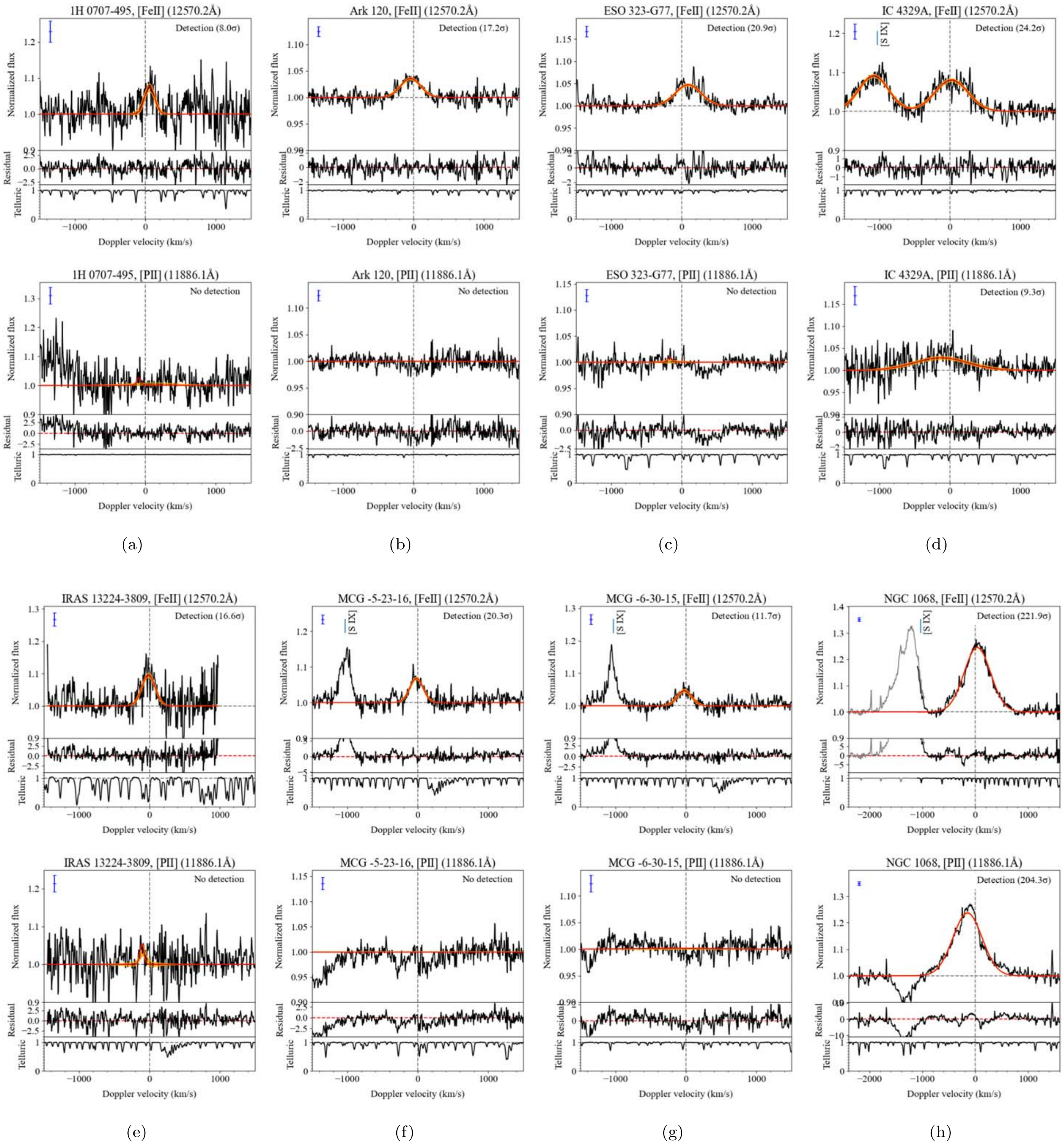

(a) (b) (c) (d)

(e) (f) (g) (h)

Figure 3. Velocity profiles of the [Fe II] and [P II] emission lines. Positive velocities mean redshift, and negative velocities indicate blueshift. The red line in each panel shows the model (continuum + Gaussian) when the parameter with the maximum likelihood in the sampling is adopted. The orange shade shows the 1σ posterior spread from the median sampling for each wavelength bin. The middle and bottom panels show the residuals and the telluric absorption, respectively. The blue bar in the upper left corner shows the typical error on the continuum. The gray bar shows the spectrum in the adjacent Echelle order. The adjacent [S IX] line is labeled. When the line is detected, its significance is written in the upper right corner. (a) 1H 0707−495, (b) Ark 120, (c) ESO 323-G77, (d) IC 4329A, (e) IRAS 13224−3809, (f) MCG −5-23-16, (g) MCG −6-30-15, and (h) NGC 1068. In NGC 4507, the adjacent [S IX] line is introduced as the solid gray line. (i) NGC 1365, (j) NGC 3783, (k) NGC 4507, (l) NGC 6240, and (m) NGC 7582. When an additional Gaussian was necessary, each Gaussian component is shown as a dotted blue line.

4.4. Future Work

In our observations, some AGNs exhibit [P II] lines that are too weak to be detected, necessitating the calculation of upper limits on the [Fe II]/[P II] ratios alone. In these cases, firm conclusions regarding the presence of shocks for these targets are elusive. Therefore, it is necessary to employ multiple diagnostic methods to confirm the existence of shocks. For

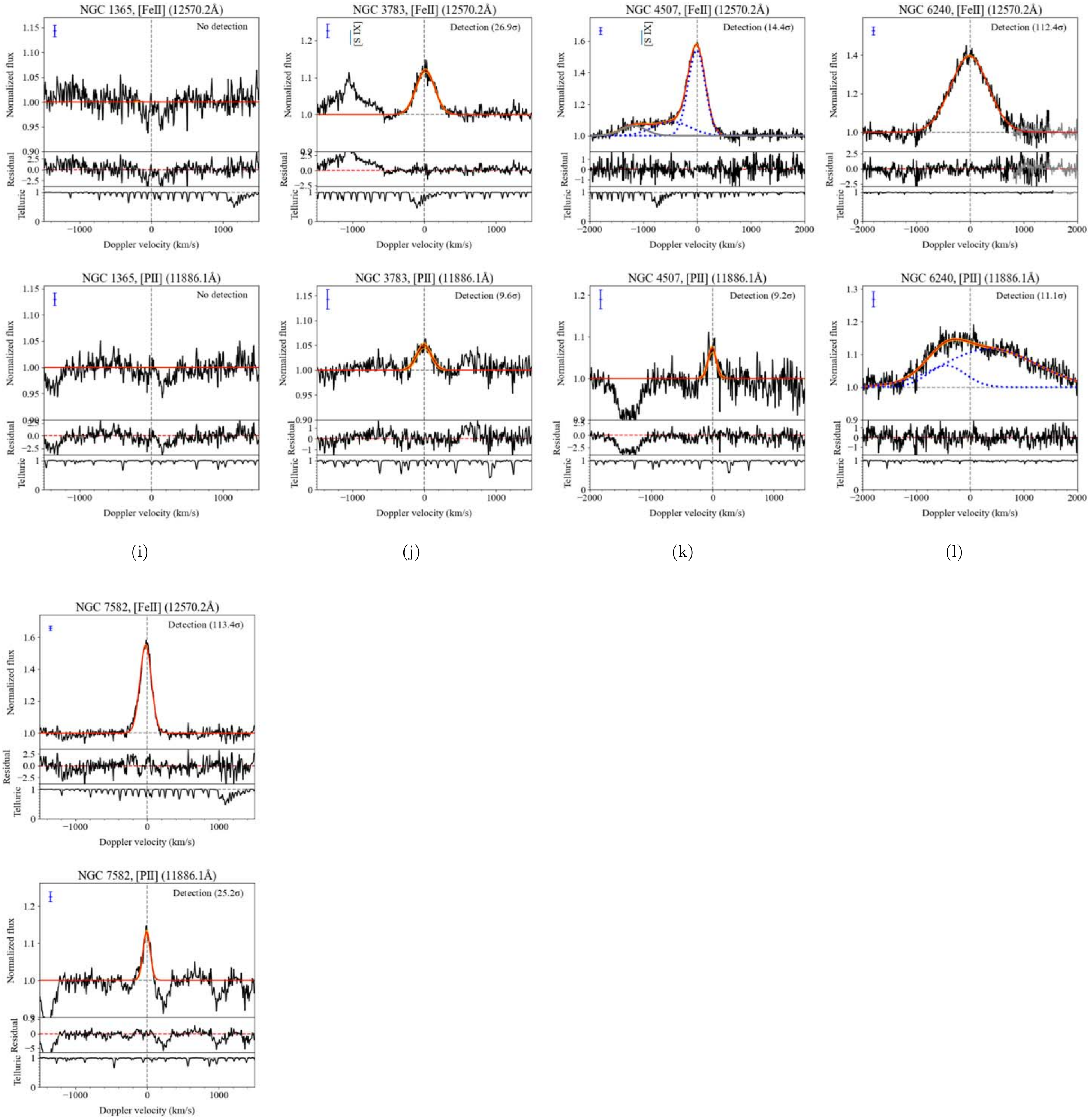

(i) (j) (k) (l)

(m)

Figure 3. (Continued.)

instance, Figure 13 in Calabrò et al. (2023) introduced various diagnostic diagrams to identify the shock. Among these, the [S III] 9530 Å /Paγ versus [Fe II] 1.257 μm/Paβ diagram can be constructed based on our WINERED observations. Our subsequent publications will provide comprehensive spectral data, including full spectra, line profiles, and EWs, encompassing Paβ and Paγ.

Spatially resolved observations of [Fe II], [P II], and [S III] play a pivotal role in elucidating the ionization mechanism within the NLR and facilitating direct observations of energy transfer from the AGN to kiloparsec-scale regions. Some previous studies have generated [Fe II] and [P II] maps within the NLR context (Storchi-Bergmann et al. 2009; Riffel et al. 2014; Fazeli & Busch 2019; Schönell et al. 2019; Riffel et al. 2020, 2021). For instance, Schönell et al. (2019) presented [Fe II]/[P II] maps for six nearby AGNs, highlighting that NGC 3227 and NGC 5899 exhibit peak values that are offset from the nuclear position and are aligned with the high-velocity

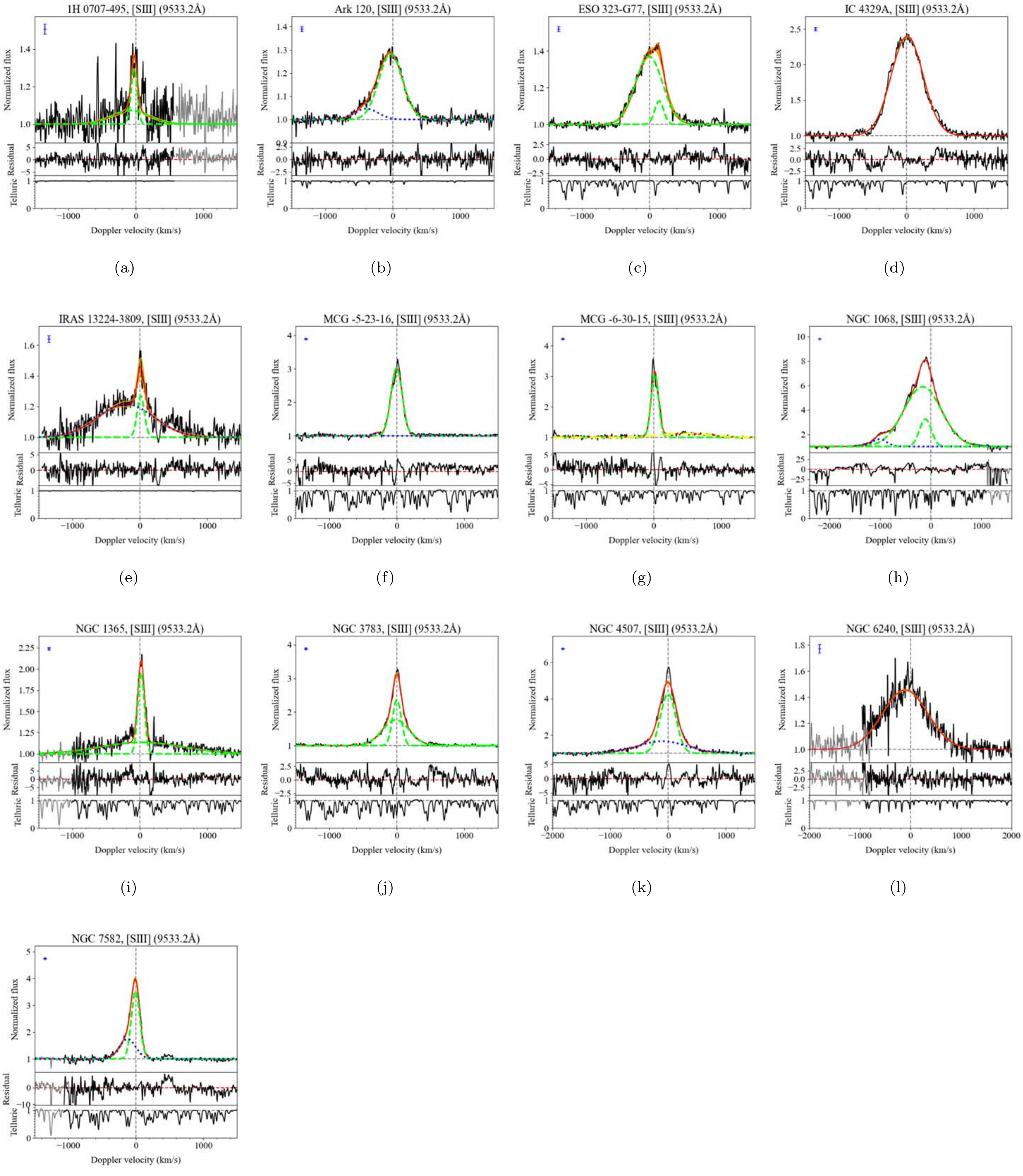

(a) (b) (c) (d)

(e) (f) (g) (h)

(i) (j) (k) (l)

(m)

Figure 4. Velocity profiles of the [S III] emission lines. The solid gray line shows the spectrum in the adjacent Echelle order. Gaussians whose central velocity is $v = 0$ within 3σ are shown as dashed green lines, whereas those on the blue side (blue wing) are shown as dotted blue lines. The exception is MCG −6-30-15, which shows an excess on the red side (yellow dot–dashed line). The other notations are the same as in Figure 3.

dispersion of [Fe II]. However, the sample size remains limited, underscoring the significance of our study in expanding the roster of suitable candidates for observations like this.

The schematic diagram depicted in Figure 10 is closely aligned with theoretical shock models (King 2010; Faucher-Giguère & Quataert 2012; Faucher-Giguère et al. 2012;

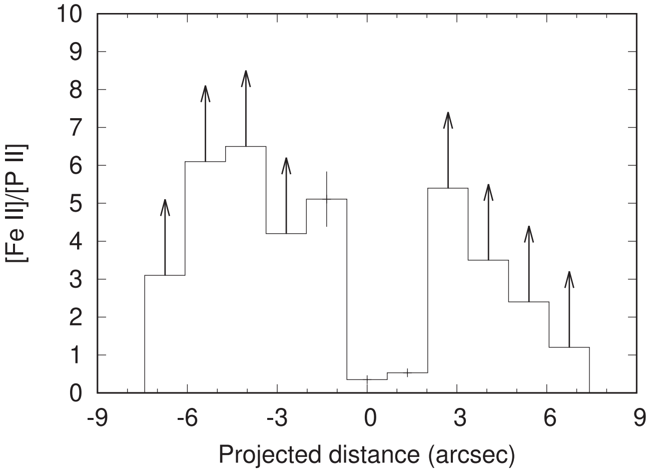

Figure 5. The [Fe II]/[P II] ratio in NGC 1068 as a function of projected distance from the core, i.e., the continuum peak. The positive direction was determined to be northwest.

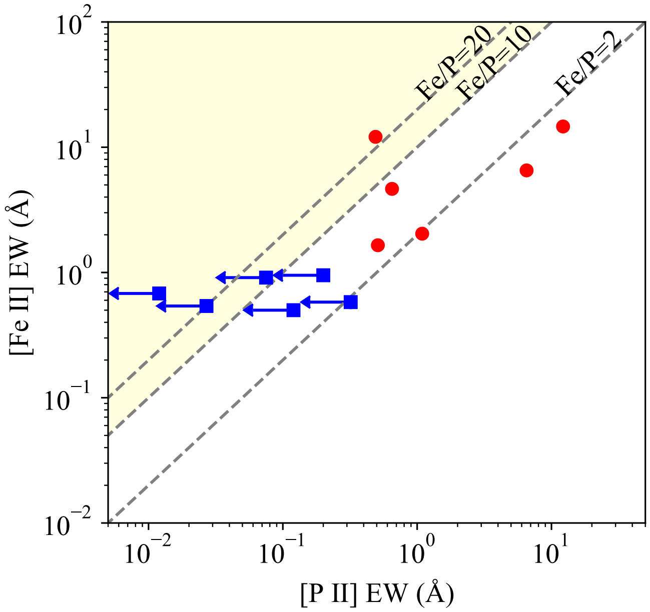

Figure 6. Relation between the EWs of [Fe II] and [P II]. The red points show the targets for which both the [Fe II] and [P II] lines are detected, and the blue points show those without a detection of [P II]. The dashed lines show [Fe II]/[P II] = 2, 10, and 20. The yellow shaded area shows the shock region.

Zubovas & King 2012; King & Pounds 2015; Richings & Faucher-Giguère 2018a, 2018b; Zubovas & King 2019). In these models, the inner radiation-driven wind interacts with the ISM, giving rise to a shock front. This shock front subsequently sweeps up the ISM, generating a region of shocked ISM. The nature of this shock hinges on whether cooling, typically radiation, significantly dissipates energy from the hot shocked gas on a timescale shorter than its flow time. If cooling exerts a strong influence in this context, most of the preshock kinetic energy is lost via radiation, characterizing a momentum-driven flow. Intense cooling results in a substantial compression of the shocked gas, yielding a geometrically narrow postshock region. Conversely, in scenarios where cooling is negligible, the postshock gas retains all the mechanical energy imparted by the shock and undergoes adiabatic expansion into the ISM. In

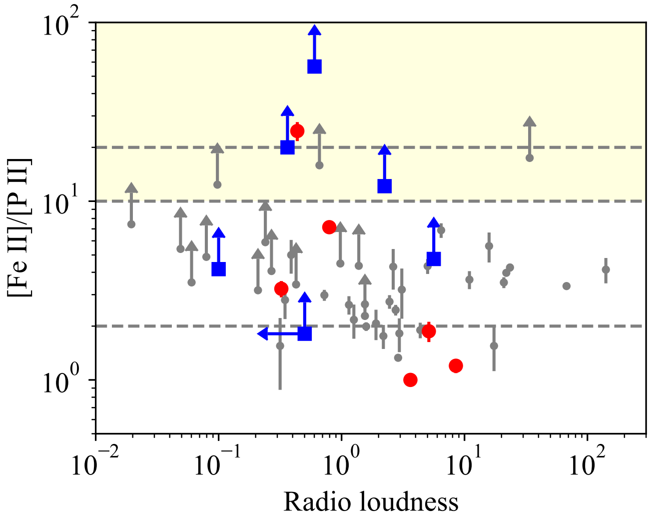

Figure 7. Relation between the [Fe II]/[P II] ratio and the radio-loudness. The notations are the same as in Figure 6. The results of T16 are superposed in gray. We find no correlation between the shocks and radio-loudness.

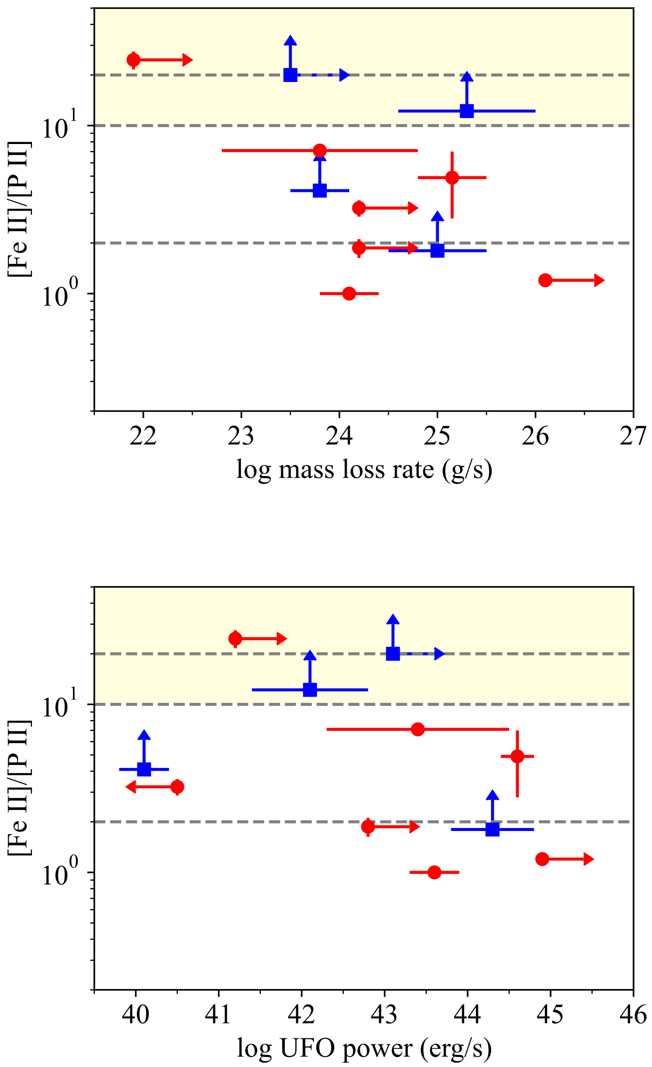

Figure 8. Relation between the [Fe II]/[P II] ratio and the UFO mass-loss rate (in the upper panel) and kinetic power (in the lower panel). The notations are the same as in Figure 6. No correlation between the shock and the UFO parameter is visible.

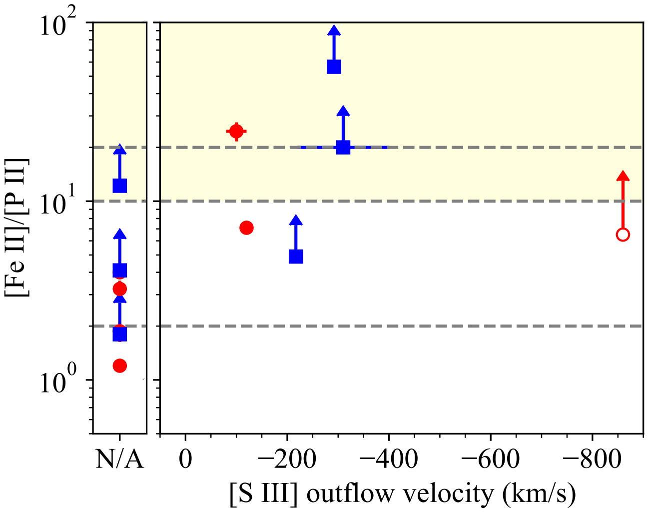

Figure 9. Relation between the [Fe II]/[P II] ratio and the [S III] outflow velocity. The outflow velocity of the targets without an [S III] outflow is set to 0. The open red circle shows NGC 1068, but off-centered (where the projected distance is $\sim -3''$; see Figure 5). The other notations are the same as in Figure 6.

contrast to the momentum-driven (isothermal) case, the postshock gas in energy-driven flows is characterized by a geometrically elongated structure. Given that energy-driven flows are significantly more intense than momentum-driven flows, the assessment of the impact of radiative outflows on the surrounding environment (in this case, the NLR) hinges on the type of gas flow described above. To unravel these complexities, it is essential to measure momentum fluxes before and after the shock, necessitating an accurate assessment of the spatial scales. Therefore, spatially resolved observations as outlined in the preceding paragraph assume paramount importance.

5. Conclusion

We performed NIR slit spectroscopy of 13 Seyfert galaxies for which UFOs have been observed in X-rays and measured their [Fe II]/[P II] ratio, with the aim of determining whether AGN outflows can generate shocks in the NLR. The [Fe II] and [P II] lines were detected in 12 and 6 of the sources, respectively. From the derived ratios, we found that shocks are likely to be present in 4 objects, Ark 120, ESO 323-G77, MCG −5-23-16, and NGC 4507. No direct relation between the presence or absence of the shocks and UFOs is found. On the other hand, we found that when the [Fe II]/[P II] ratio is higher than ~7, the [S III] emission line shows signs of ionized outflow. We favor a scenario in which the ionized outflows trigger the NLR-scale shock. The scenario has been evaluated so far only for NGC 1068, using the IFU observation, before this work. This work revealed that the scenario is likely to be applicable for a wider sample range.

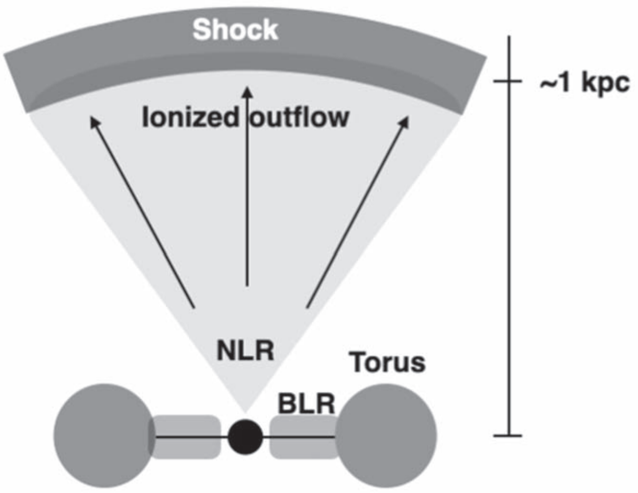

Figure 10. Schematic picture of the ionized outflow, NLR, and shock region. For NGC 1068, the ionized outflow is traced in the [O III] and [S III] lines. The outer radius of the ionized outflow matches the radius of the shock-dominant annulus.

Acknowledgments

This study is based on observations collected at the European Southern Observatory under ESO program 0100.B-0798(A). We are deeply grateful to the NTT and La Silla team in ESO for their technical support. This study was financially supported by the Hayakawa Fund in Astronomical Society of Japan (M.M.), and Grants-in-Aid, KAKENHI, from Japan Society for the Promotion of Science (JSPS) Nos. JP21K13958 (M.M.) and JP19K03917 (H.S.). The WINERED was developed by the University of Tokyo and the Laboratory of Infrared High-resolution Spectroscopy (LiH), Kyoto Sangyo University under the financial supports of JSPS KAKENHI Nos. JP16684001 (N.K.), JP20340042 (N.K.), JP21840052 (Y.I.), and the MEXT Supported Program for the Strategic Research Foundation at Private Universities, Nos. S0801061 and S1411028 (H.K.). N.K. appreciates the support from JSPS-DST under the Japan-India Science Cooperative Programs during 2013–2015 and 2016–2018.

Facility: NTT.

Software: WINERED pipeline (S. Hamano et al. 2023, in preparation), IRAF (Tody 1986, 1993), PyRAF (Science Software Branch at STScI 2012).

Appendix A
Line Profiles of Each Object

This appendix describes the line profiles of the [Fe II], [P II], and [S III] lines, and other emission or absorption-like features, if any, of individual sources (Figures 3 and 4).

A.1. 1H 0707−495

The data for 1H 0707−495 have the lowest signal-to-noise ratio of the observed target sources, $S/N \sim 15$–20 at the continuum level. The [Fe II] emission line was detected and fit with a single Gaussian, but not for [P II]. Some residuals are seen around $-1400\ \mathrm{km\ s^{-1}}$ of the [P II] line, the origin of which is unknown. The [S III] line has a narrow core ($\sigma_v = 46 \pm 3\ \mathrm{km\ s^{-1}}$) and broad emission ($\sigma_v = 280 \pm 30\ \mathrm{km\ s^{-1}}$).

A.2. Ark 120

At the [P II] wavelengths, no emission lines are detected, but rather a slight absorption structure can be seen. The [S III] blue wing is present at $-310 \pm 90\ \mathrm{km\ s^{-1}}$.

A.3. ESO 323-G77

The [S III] line shows an asymmetric profile and is well fit with two Gaussians; the main Gaussian has $\sigma_v = 203 \pm 4\,\mathrm{km\,s^{-1}}$ and the sub-Gaussian has a line shift of $+144 \pm 9\,\mathrm{km\,s^{-1}}$ and $\sigma_v = 75 \pm 11\,\mathrm{km\,s^{-1}}$.

A.4. IC 4329A

The [S IX]λ12520 line is present in addition to the standard lines and an additional Gaussian is required to fit the [Fe II] line properly.

A.5. IRAS 13224−3809

The data of both the [Fe II] and [P II] lines appear noisy due to a low signal-to-noise ratio and heavy telluric absorption. A hint of the [P II] emission line is seen at $v = -100\,\mathrm{km\,s^{-1}}$, but its strength ($2.78\sigma$) is below the detection threshold.

A.6. MCG −5-23-16

The [S IX]λ12520 line is also present in addition to the standard lines. Three absorption lines are observed in the [P II] band: −1400, −200, and $+200\,\mathrm{km\,s^{-1}}$. Their line widths are broader than those in the telluric lines. In particular, the broadest line is at $-1400\,\mathrm{km\,s^{-1}}$ (11830 Å). The upper limit of the [P II] is well constrained. The [S III] line shows slight absorption at the center, which might also be due to the two narrow emission lines constituting the central peak. We fit it with a single positive Gaussian.

A.7. MCG −6-30-15

The [S IX]λ12520 line appears to have a blue wing. Absorption features are present at −1400 and $+100\,\mathrm{km\,s^{-1}}$ of the [P II] line. The [S III] line has a redshifted broad emission line, the physical origin of which is unknown.

A.8. NGC 1068

NGC 1068 is the nearest of our targets. It shows the largest [P II] EW and σ_v and lowest [Fe II]/[P II] ratio. The central peak of [P II] is shifted by $-200\,\mathrm{km\,s^{-1}}$ from that of [Fe II]. An absorption feature at $-1400\,\mathrm{km\,s^{-1}}$ is also present in the [P II] band. The [S III] outflow has the fastest velocity of our targets, $-840\,\mathrm{km\,s^{-1}}$.

A.9. NGC 1365

Neither of the [Fe II] and [P II] lines is detected. The [Fe II] band has two absorption features at −50 and $+200\,\mathrm{km\,s^{-1}}$, and the [P II] band has features at −1400 and $+200\,\mathrm{km\,s^{-1}}$. The presence of the $+200\,\mathrm{km\,s^{-1}}$ features may be due either to the Doppler motion of the lines or it might simply be a positional coincidence. The [S III] line was modeled with two Gaussians: a narrower Gaussian ($\sigma_v = 49 \pm 5\,\mathrm{km\,s^{-1}}$), and a broader Gaussian ($\sigma_v = 620 \pm 40\,\mathrm{km\,s^{-1}}$). The broader Gaussian is slightly redshifted, but within the error bar ($+17 \pm 18\,\mathrm{km\,s^{-1}}$).

A.10. NGC 3783

The wavelength range for the [Fe II] lines of this source overlaps with that with heavy telluric absorption. Nevertheless, the wavelength resolution is sufficiently good to enable us to remove the effect. The [S IX]λ12520 line seems to have a red wing, in contrast to that of MCG −6-30-15. A positive residual remains from +500 to $+800\,\mathrm{km\,s^{-1}}$ of the [P II] line, whose origin is unknown. The [S III] line profile is reproduced with two positive Gaussians: a narrower Gaussian ($\sigma_v = 65 \pm 2\,\mathrm{km\,s^{-1}}$), and a broader Gaussian ($\sigma_v = 200 \pm 3\,\mathrm{km\,s^{-1}}$).

A.11. NGC 4507

The blue wing is seen in [Fe II] and is merged with the [S IX] line. Therefore, the fitting requires three Gaussians, the [Fe II] core ($\sigma_v = 151 \pm 2\,\mathrm{km\,s^{-1}}$), the [Fe II] wing ($v = -481 \pm 4\,\mathrm{km\,s^{-1}}$ and $\sigma_v = 583 \pm 16\,\mathrm{km\,s^{-1}}$), and the [S IX] line. The [S III] line also shows a blue wing at $-100 \pm 20\,\mathrm{km\,s^{-1}}$ with $\sigma_v = 420 \pm 120\,\mathrm{km\,s^{-1}}$. Considering that the [P II] line has no indication of a blue wing, some shock due to the outflow is expected in this target. We also note that a strong absorption is present in the [P II] band ($-1400\,\mathrm{km\,s^{-1}}$).

A.12. NGC 6240

NGC 6240 is a merging luminous infrared galaxy and has two cores. In this study, the brighter southern core was observed in the slit. The [Fe II] and [P II] lines are both strong and broad. In particular, the [P II] line profile required two Gaussian components with $v = 400 \pm 80/-440 \pm 30\,\mathrm{km\,s^{-1}}$ and $\sigma_v = 850 \pm 50/370 \pm 40\,\mathrm{km\,s^{-1}}$. The [S III] line has a similar line broadening as the [Fe II] line.

A.13. NGC 7582

The absorption features are observed at around the [P II] line at −1400, +200, and $+1000\,\mathrm{km\,s^{-1}}$. The [S III] blue wing is detected at $-120\,\mathrm{km\,s^{-1}}$.

Appendix B
Corner Plots for the [Fe II] and [P II] Line Fitting

We fit the [Fe II] and [P II] lines with Gaussians. Figure 11 displays the corner plots in the MCMC fitting shown in Figure 3. The Gaussian amplitudes, central velocity, and velocity dispersion are shown. For [Fe II] in NGC 4507 and [P II] in NGC 6240, only the results for the Gaussian with the largest EW are shown.

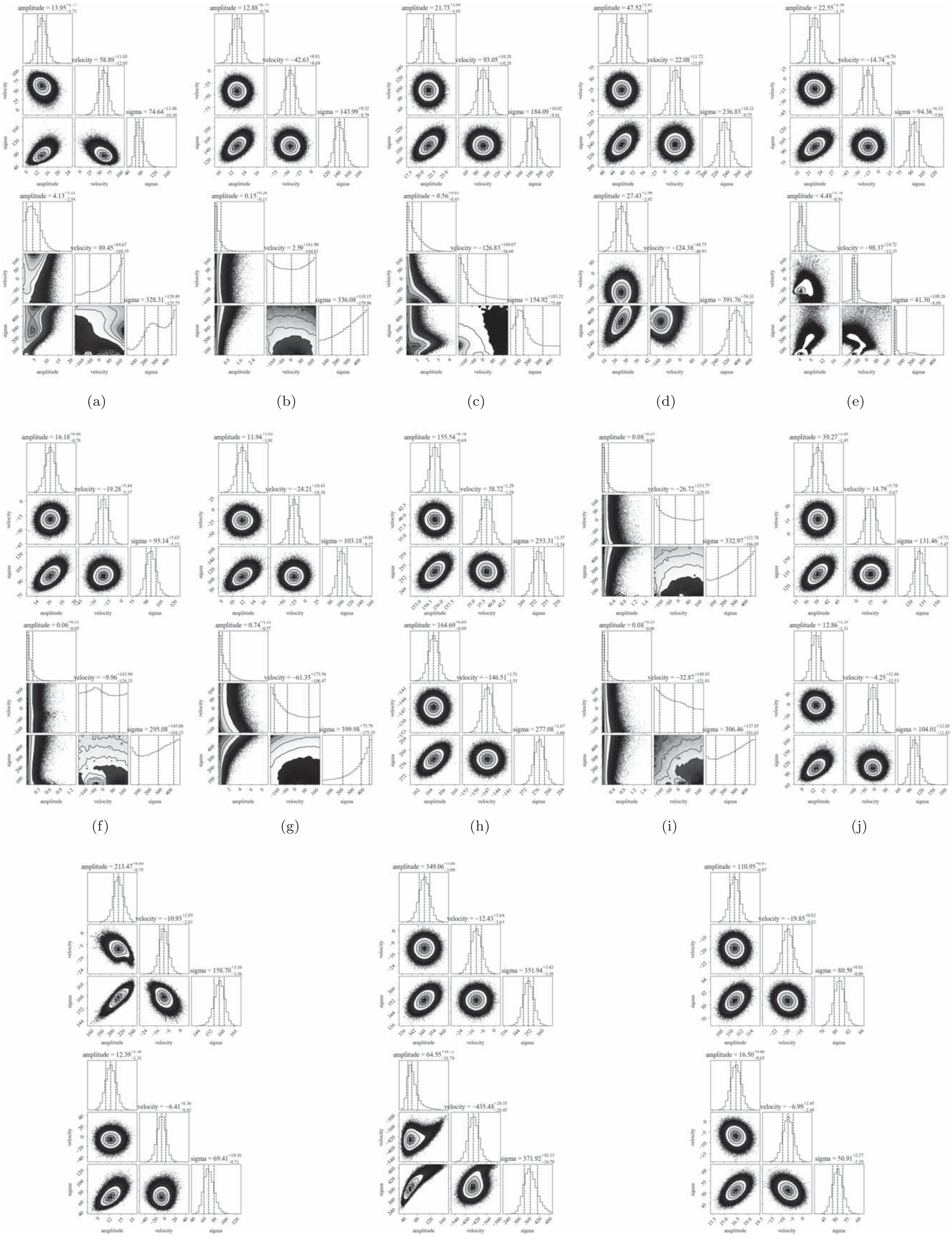

(a) (b) (c) (d) (e)

(f) (g) (h) (i) (j)

(k) (l) (m)

Figure 11. Corner plots for the [Fe II] (upper panel) and [P II] (lower panel) line fitting in Figure 3. See the caption of Figure 3 for the target name.

ORCID iDs

Misaki Mizumoto https://orcid.org/0000-0003-2161-0361
Hiroaki Sameshima https://orcid.org/0000-0001-6401-723X
Naoto Kobayashi https://orcid.org/0000-0003-4578-2619
Satoshi Hamano https://orcid.org/0000-0002-6505-3395
Chikako Yasui https://orcid.org/0000-0003-3579-7454
Kei Fukue https://orcid.org/0000-0003-2516-9753
Akira Arai https://orcid.org/0000-0002-5756-067X
Hideyo Kawakita https://orcid.org/0000-0003-2011-9159
Giuseppe Bono https://orcid.org/0000-0002-4896-8841
Ivo Saviane https://orcid.org/0000-0002-5878-5299

References

Appleby, S., Davé, R., Kraljic, K., Anglés-Alcázar, D., & Narayanan, D. 2020, MNRAS, 494, 6053
Bevington, P. R. 1969, Data Reduction and Error Analysis for the Physical Sciences (New York: McGraw-Hill)
Booth, C. M., & Schaye, J. 2009, MNRAS, 398, 53
Calabrò, A., Pentericci, L., Feltre, A., et al. 2023, A&A, 679, A80
Chartas, G., & Canas, M. H. 2018, ApJ, 867, 103
Crain, R. A., Schaye, J., Bower, R. G., et al. 2015, MNRAS, 450, 1937
Das, V., Crenshaw, D. M., Kraemer, S. B., & Deo, R. P. 2006, AJ, 132, 620
Davé, R., Anglés-Alcázar, D., Narayanan, D., et al. 2019, MNRAS, 486, 2827
Davies, R., Baron, D., Shimizu, T., et al. 2020, MNRAS, 498, 4150
Eadie, W. T., Drijard, D., & James, F. E. 1971, Statistical Methods in Experimental Physics (Amsterdam: North-Holland)
Faucher-Giguère, C. A., & Quataert, E. 2012, MNRAS, 425, 605
Faucher-Giguère, C. A., Quataert, E., & Murray, N. 2012, MNRAS, 420, 1347
Fazeli, N., Busch, G., et al. 2019, A&A, 622, A128
Ferrarese, L., & Merritt, D. 2000, ApJL, 539, L9
Foreman-Mackey, D., Hogg, D. W., Lang, D., & Goodman, J. 2013, PASP, 125, 306
Gebhardt, K., Bender, R., Bower, G., et al. 2000, ApJL, 539, L13
Glikman, E., Helfand, D. J., & White, R. L. 2006, ApJ, 640, 579
Gofford, J., Reeves, J. N., McLaughlin, D. E., et al. 2015, MNRAS, 451, 4169
Gofford, J., Reeves, J. N., Tombesi, F., et al. 2013, MNRAS, 430, 60
Hagino, K., Odaka, H., Done, C., et al. 2016, MNRAS, 461, 3954
Harrison, C. M., Alexander, D. M., Mullaney, J. R., & Swinbank, A. M. 2014, MNRAS, 441, 3306
Harrison, C. M., Costa, T., Tadhunter, C. N., et al. 2018, NatAs, 2, 198
Hashimoto, T., Nagao, T., Yanagisawa, K., Matsuoka, K., & Araki, N. 2011, PASJ, 63, L7
Ho, L. C., Shields, J. C., & Filippenko, A. V. 1993, ApJ, 410, 567
Hobbs, L. M., Welty, D. E., Morton, D. C., Spitzer, L., & York, D. G. 1993, ApJ, 411, 750
Hönig, S. F., Kishimoto, M., Tristram, K. R. W., et al. 2013, ApJ, 771, 87
Ikeda, Y., Kobayashi, N., Kondo, S., et al. 2016, Proc. SPIE, 9908, 99085Z
Ikeda, Y., Kondo, S., Otsubo, S., et al. 2022, PASP, 134, 015004
Intema, H. T., Jagannathan, P., Mooley, K. P., & Frail, D. A. 2017, A&A, 598, A78
Joh, K., Nagao, T., Wada, K., Terao, K., & Yamashita, T. 2021, PASJ, 73, 1152
Karouzos, M., Woo, J. H., & Bae, H. J. 2016, ApJ, 819, 148
King, A., & Pounds, K. 2015, ARA&A, 53, 115
King, A. R. 2010, MNRAS, 402, 1516
King, A. R., & Pounds, K. A. 2003, MNRAS, 345, 657
Knop, R. A., Armus, L., Larkin, J. E., et al. 1996, AJ, 112, 81
Komossa, S., Xu, D., Zhou, H., Storchi-Bergmann, T., & Binette, L. 2008, ApJ, 680, 926
Lee, J. C., Ogle, P. M., Canizares, C. R., et al. 2001, ApJL, 554, L13
Leftley, J. H., Tristram, K. R. W., Hönig, S. F., et al. 2018, ApJ, 862, 17
Liu, G., Arav, N., & Rupke, D. S. N. 2015, ApJS, 221, 9
Liu, G., Zakamska, N. L., Greene, J. E., Nesvadba, N. P. H., & Liu, X. 2013, MNRAS, 430, 2327
Marasco, A., Cresci, G., Nardini, E., et al. 2020, A&A, 644, A15
Meena, B., Crenshaw, D. M., Schmitt, H. R., et al. 2021, ApJ, 916, 31
Mizumoto, M., Izumi, T., & Kohno, K. 2019, ApJ, 871, 156
Mouri, H., Kawara, K., & Taniguchi, Y. 2000, ApJ, 528, 186
Müller-Sánchez, F., Prieto, M. A., Hicks, E. K. S., et al. 2011, ApJ, 739, 69
Nelson, D., Pillepich, A., Springel, V., et al. 2019, MNRAS, 490, 3234
Noll, S., Kausch, W., Kimeswenger, S., et al. 2014, A&A, 567, A25
Oliva, E., Marconi, A., Maiolino, R., et al. 2001, A&A, 369, L5
Parker, M. L., Pinto, C., Fabian, A. C., et al. 2017, Natur, 543, 83
Peterson, B. M. 1997, An Introduction to Active Galactic Nuclei (Cambridge: Cambridge Univ. Press)
Pillepich, A., Springel, V., Nelson, D., et al. 2018, MNRAS, 473, 4077
Pounds, K. A., Reeves, J. N., King, A. R., et al. 2003, MNRAS, 345, 705
Reeves, J. N., O'Brien, P. T., & Ward, M. J. 2003, ApJL, 593, L65
Richings, A. J., & Faucher-Giguère, C.-A. 2018a, MNRAS, 474, 3673
Richings, A. J., & Faucher-Giguère, C. A. 2018b, MNRAS, 478, 3100
Riffel, R. A., Bianchin, M., Riffel, R., et al. 2021, MNRAS, 503, 5161
Riffel, R. A., Storchi-Bergmann, T., Zakamska, N. L., & Riffel, R. 2020, MNRAS, 496, 4857
Riffel, R. A., Vale, T. B., Storchi-Bergmann, T., & McGregor, P. J. 2014, MNRAS, 442, 656
Rodríguez-Ardila, A., Pastoriza, M. G., Viegas, S., Sigut, T. A. A., & Pradhan, A. K. 2004, A&A, 425, 457
Rupke, D. S., Veilleux, S., & Sanders, D. B. 2005, ApJS, 160, 115
Sameshima, H., Matsunaga, N., Kobayashi, N., et al. 2018, PASP, 130, 074502
Schaye, J., Crain, R. A., Bower, R. G., et al. 2015, MNRAS, 446, 521
Schönell, A. J., Storchi-Bergmann, T., Riffel, R. A., et al. 2019, MNRAS, 485, 2054
Science Software Branch at STScI, 2012 PyRAF: Python alternative for IRAF, Astrophysics Source Code Library, ascl:1207.011
Simpson, C., Ward, M., Clements, D. L., & Rawlings, S. 1996, MNRAS, 281, 509
Singha, M., Husemann, B., Urrutia, T., et al. 2022, A&A, 659, A123
Storchi-Bergmann, T., McGregor, P. J., Riffel, R. A., et al. 2009, MNRAS, 394, 1148
Terao, K., Nagao, T., Hashimoto, T., et al. 2016, ApJ, 833, 190
Thomas, N., Davé, R., Anglés-Alcázar, D., & Jarvis, M. 2019, MNRAS, 487, 5764
Tody, D. 1986, Proc. SPIE, 627, 733
Tody, D. 1993, in ASP Conf. Ser. 52, Astronomical Data Analysis Software and Systems II, ed. R. J. Hanisch, R. J. V. Brissenden, & J. Barnes (San Francisco, CA: ASP), 173
Tombesi, F., Cappi, M., Reeves, J. N., et al. 2010, A&A, 521, A57
Tombesi, F., Cappi, M., Reeves, J. N., & Braito, V. 2012, MNRAS, 422, L1
Tombesi, F., Meléndez, M., Veilleux, S., et al. 2015, Natur, 519, 436
Tombesi, F., Tazaki, F., Mushotzky, R. F., et al. 2014, MNRAS, 443, 2154
Trippe, M. L., Crenshaw, D. M., Deo, R. P., et al. 2010, ApJ, 725, 1749
Véron-Cetty, M. P., & Véron, P. 2010, A&A, 518, A10
Wada, K., Yonekura, K., & Nagao, T. 2018, ApJ, 867, 49
Weinberger, R., Springel, V., Hernquist, L., et al. 2017, MNRAS, 465, 3291
Weinberger, R., Springel, V., Pakmor, R., et al. 2018, MNRAS, 479, 4056
Wilson, A. S., & Raymond, J. C. 1999, ApJL, 513, L115
Zubovas, K., & King, A. 2012, ApJL, 745, L34
Zubovas, K., & King, A. R. 2019, GReGr, 51, 65